

The effect of the adiabatic assumption on asteroseismic scaling relations for luminous red giants

JOEL C. ZINN,^{1, 2, 3, 4,*} MARC H. PINSONNEAULT,³ LARS BILDSTEN,⁵ AND DENNIS STELLO^{2, 6, 7, 8}

¹ Department of Astrophysics, American Museum of Natural History, Central Park West at 79th Street, New York, NY 10024, USA

² School of Physics, University of New South Wales, Barker Street, Sydney, NSW 2052, Australia

³ Department of Astronomy, The Ohio State University, 140 West 18th Avenue, Columbus, OH 43210, USA

⁴ Kavli Institute for Theoretical Physics, University of California, Santa Barbara, CA 93106, USA

⁵ Kavli Institute for Theoretical Physics and Department of Physics Kohn Hall, University of California, Santa Barbara, CA 93106, USA

⁶ Sydney Institute for Astronomy (SIfA), School of Physics, University of Sydney, NSW 2006, Australia

⁷ Stellar Astrophysics Centre, Department of Physics and Astronomy, Aarhus University, Ny Munkegade 120, DK-8000 Aarhus C, Denmark

⁸ Center of Excellence for Astrophysics in Three Dimensions (ASTRO-3D), Australia

ABSTRACT

Although stellar radii from asteroseismic scaling relations agree at the percent level with independent estimates for main sequence and most first-ascent red giant branch stars, the scaling relations seem to over-predict radii at the tens of percent level for the most luminous stars ($R \gtrsim 30R_{\odot}$). These evolved stars have significantly non-adiabatic outer envelopes, and the extent of these regions increase with increasing radius at fixed mass and metallicity. However, adiabaticity is assumed in the theoretical derivation of the asteroseismic scaling relations. The adiabatic approximation is also assumed in theoretical corrections to observed frequencies via so-called ‘surface corrections’ and the large frequency separation corrections. Here, we show that a part of the asteroseismic radius scale inflation may arise from this assumption of adiabaticity. With a new reduction of Kepler asteroseismic data, we find that stars with $R \lesssim 30R_{\odot}$ have asteroseismic scaling relation radii that are accurate to within at least 2% compared to Gaia radii, when treated in the adiabatic assumption. The accuracy of asteroseismic radii for stars with $R \gtrsim 50R_{\odot}$, however, is not better than 10% – 15% using adiabatic large frequency separation corrections. We find that up to 4% of this disagreement could be caused by the adiabatic assumption, which we predict would increase to 10% for stars even closer to the tip of the red giant branch. We discuss physical origins of the importance of non-adiabaticity in these luminous giants, which are related to the efficiency of convection. Taking into account non-adiabaticity in red giants, as we argue, is increasingly important to properly model these stars even outside of the asteroseismic context, and will require more computationally expensive physics to treat these large non-adiabatic regions using, e.g., patched hydrodynamic convection simulations and radiative transport atmospheres.

1. INTRODUCTION

1.1. Adiabatic asteroseismic scaling relations for ensemble asteroseismology

Ensemble asteroseismology has flourished following the space-based missions of CoRoT (Baglin et al. 2006), Kepler (Borucki et al. 2008), and K2 (Howell et al. 2014), which have provided tens of thousands of red giant asteroseismic detections (e.g., de Assis Peralta et al. 2018; Yu et al. 2018; Stello et al. 2017). With TESS (Ricker et al. 2014) expected to deliver hundreds of thousands of

red giant asteroseismic detections (Aguirre et al. 2020; Hon et al. 2021), and PLATO (Rauer et al. 2014) also delivering a similar number (Mosser et al. 2019), ensuring that asteroseismic parameters are accurate is crucial for stellar physics and Galactic archaeology.

The equations governing stellar pulsations are derived by linearizing stellar structure equations that have been perturbed around the equilibrium solution. This linearization has largely followed the adiabatic perturbative analysis of Tassoul (1980) (in the tradition of adiabatic approximations of Pekeris (1938) and Cowling (1941)). In this treatment, the fully general heat equation,

$$\frac{dq}{dt} = \frac{1}{\rho(\Gamma_3 - 1)} \left(\frac{dp}{dt} - \frac{\Gamma_1 p}{\rho} \frac{d\rho}{dt} \right) \quad (1)$$

Corresponding author: Joel C. Zinn

jzinn@amnh.org

* NSF Astronomy and Astrophysics Postdoctoral Fellow.

is traditionally approximated under the assumption that there is no heat gain or loss ($\frac{dq}{dt} = 0$), and so the adiabatic expression for how pressure and density variations are related to each other is recovered:

$$\frac{dp}{dt} = \frac{\Gamma_1 p}{\rho} \frac{d\rho}{dt}. \quad (2)$$

The effect of the adiabatic approximation on inferred stellar parameters has been quantified for red giant branch stars in a very narrow range of stellar radius (2.47-2.77 R_\odot) by [Buldgen et al. \(2019\)](#) for asteroseismic inversions. An exploration for more luminous giants has not been done, nor has the adiabatic error been quantified for asteroseismic scaling relations, which are used in ensemble asteroseismic analysis of thousands of stars (e.g., from TESS or K2). Compared to asteroseismic inversions that use the frequencies of all observed modes to constrain stellar models, asteroseismic scaling relations yield stellar radius and mass using only two characteristic frequencies in a solar-like oscillator spectrum: $\Delta\nu$ and ν_{\max} .

Regarding $\Delta\nu$, [Tassoul \(1980\)](#) showed that the solution of the resulting stellar pulsation equations have eigenvalue solutions (corresponding to mode frequencies) that are regularly separated in frequency space. In particular, the separation of modes of the same degree but adjacent radial order in the limit of large radial order, is given by the so-called large frequency separation ([Ulrich 1986; Kjeldsen & Bedding 1995](#)):

$$\frac{\Delta\nu}{\Delta\nu_\odot} \approx \sqrt{\frac{M/M_\odot}{(R/R_\odot)^3}}. \quad (3)$$

The frequency at maximum power, ν_{\max} , is known both empirically and theoretically to be related to the pressure scale height in the stellar atmosphere, and therefore to stellar surface gravity and effective temperature ([Brown et al. 1991; Kjeldsen & Bedding 1995; Chaplin et al. 2008; Belkacem et al. 2011](#)):

$$\frac{\nu_{\max}}{\nu_{\max,\odot}} \approx \frac{M/M_\odot}{(R/R_\odot)^2 \sqrt{(T_{\text{eff}}/T_{\text{eff},\odot})}}. \quad (4)$$

1.2. Quantifying scaling relation errors with $f_{\Delta\nu}$ and $f_{\nu_{\max}}$

There has been a consensus in recent years that the observed $\Delta\nu$ does not exactly follow the scaling relation (e.g., [Stello et al. 2009](#)), which has been understood to be because Equation 3 is valid only when $\Delta\nu$ corresponds to the frequency separation at infinitely large radial order. Of course, in practice, the observed modes in stars are not at infinitely large radial order, which

would correspond to infinitely large frequency. Though turbulent convective processes are responsible for exciting the modes, they also tend to damp high-frequency modes ([Belkacem et al. 2011](#)), meaning that the observed modes have radial order between 3-10 in red giants and between 10-30 in main sequence stars. This consideration has motivated a modified version of Equation 3:

$$\frac{\Delta\nu}{f_{\Delta\nu} \Delta\nu_\odot} \approx \sqrt{\frac{M/M_\odot}{(R/R_\odot)^3}}, \quad (5)$$

where $f_{\Delta\nu}$ captures differences in the observed $\Delta\nu$ and the $\Delta\nu$ that would be measured at infinite radial order. $f_{\Delta\nu}$ is computed by first matching a stellar structure model to an observed star, given a temperature, a metallicity, etc. A scaling relation $\Delta\nu$ can be computed directly from the model mean stellar density according to Equation 3. Model pulsation frequencies are then calculated from the stellar structure model using linearized, adiabatic stellar pulsation equations and a $\Delta\nu$ is computed using the model frequencies at low radial order in the vicinity of the observed ν_{\max} to create a model-observed $\Delta\nu$. The model scaling relation $\Delta\nu$ is then divided by the model-observed $\Delta\nu$ to yield $f_{\Delta\nu}$. Apart from the adiabatic approximation, this formalism assumes that $f_{\Delta\nu}$ will map the observed $\Delta\nu$ onto what the observed $\Delta\nu$ would be at high radial order, where the scaling relation between $\Delta\nu$ and mean stellar density in Equation 3 should hold. Following the first calculation of a temperature-dependent $f_{\Delta\nu}$ by [White et al. \(2011\)](#), other authors have identified metallicity ([Guggenberger et al. 2016](#)), and also mass- & evolutionary state-dependences ([Sharma et al. 2016](#)). The corrections are below 1% for unevolved main sequence stars and may reach 3% for more evolved stars.

The ν_{\max} scaling relation in Equation 4, unlike the one for $\Delta\nu$ in Equation 3, is independent of the linearized stellar pulsation equations, depending instead on the local physics of the atmosphere. It still assumes adiabaticity via a dependence on the local adiabatic sound speed, however, which motivates a correction factor, $f_{\nu_{\max}}$, that would encapsulate errors in the scaling relation itself due to non-adiabatic (or other) terms entering into Equation 4 and/or systematics in the measurement of ν_{\max} :

$$\frac{\nu_{\max}}{f_{\nu_{\max}} \nu_{\max,\odot}} \approx \frac{M/M_\odot}{(R/R_\odot)^2 \sqrt{(T_{\text{eff}}/T_{\text{eff},\odot})}}. \quad (6)$$

Unfortunately, ν_{\max} cannot yet be computed from stellar models at the precisions required to calculate theoretical $f_{\nu_{\max}}$ as is possible for $f_{\Delta\nu}$ (though see [Zhou et al. 2020](#) for promising progress). Here, we assume

$f_{\nu_{\max}} = 1$, though we discuss potential reasons for $f_{\nu_{\max}} \neq 1$ in §3.4.

Rearranging Equations 5 & 6 yields asteroseismic scaling relations for radii and masses:

$$\frac{R}{R_{\odot}} \approx \left(\frac{\nu_{\max}}{f_{\nu_{\max}} \nu_{\max, \odot}} \right) \left(\frac{\Delta\nu}{f_{\Delta\nu} \Delta\nu_{\odot}} \right)^{-2} \left(\frac{T_{\text{eff}}}{T_{\text{eff}, \odot}} \right)^{1/2} \quad (7)$$

and

$$\frac{M}{M_{\odot}} \approx \left(\frac{\nu_{\max}}{f_{\nu_{\max}} \nu_{\max, \odot}} \right)^3 \left(\frac{\Delta\nu}{f_{\Delta\nu} \Delta\nu_{\odot}} \right)^{-4} \left(\frac{T_{\text{eff}}}{T_{\text{eff}, \odot}} \right)^{3/2}. \quad (8)$$

The correction to $\Delta\nu$, $f_{\Delta\nu}$, thus enters into both the radius and mass scaling relation. The correction is especially important for asteroseismic ages, which, for low-mass red giants, would scale approximately like $f_{\Delta\nu}^{12}$, according to the mass-luminosity relationship for a solar-metallicity, solar-mass main sequence star (e.g., Salaris & Cassisi 2005).

$\Delta\nu$ corrections in the form of model-dependent $f_{\Delta\nu}$ appear to improve agreement between asteroseismic radii and independent radii from eclipsing binaries (Gaulme et al. 2016; Brogaard et al. 2018) and Gaia radii (Huber et al. 2017) as well as between asteroseismic masses and astrophysical priors (Epstein et al. 2014; Sharma et al. 2016). However, the corrections do not seem to be as effective in the luminous giant regime $R \gtrsim 30R_{\odot}$, where there are discrepancies between 10 – 20% in radius compared to eclipsing binary radii (Kallinger et al. 2018) and Gaia radii (Zinn et al. 2019a).

The most luminous stars have photometric variability large enough to be detected by ground-based surveys such as OGLE (e.g., Udalski et al. 2008), the All-Sky Automated Survey (Pojmanski 1997), the All-Sky Automated Survey for SuperNovae (Shappee et al. 2014), and the Zwicky Transient Facility (Bellm et al. 2019). With hundreds of thousands of light curves available for evolved red giants in ground-based observations, and hundreds of thousands more in space-based observations from TESS (e.g., Hon et al. 2021), an understanding of pulsations in these stars is achievable observationally given a proper treatment of the pulsations theoretically. Asteroseismology of the most luminous red giant branch stars — luminous asteroseismology — with these and future surveys like PLATO (Rauer et al. 2014) and Rubin Observatory (Ivezić et al. 2019) will allow Galactic archaeology studies out to tens of kiloparsecs (e.g., Auge et al. 2020), yielding distances to better precision than Gaia (e.g., Huber et al. 2017) and asteroseismic ages for stars in the outer halo and outer disc.

Given the large problems in the radius scaling relation for luminous stars ($R \gtrsim 30R_{\odot}$) noted in the literature, it is of great interest to ensure the accuracy of $f_{\Delta\nu}$ in the luminous giant regime. The adiabatic approximation, through its effect on $f_{\Delta\nu}$, is a potential area for improvement in this regard, and we explore the magnitude of its impact on $f_{\Delta\nu}$ in what follows.

2. METHODS

2.1. Stellar structure models

Asteroseismic frequency calculations require knowledge of the detailed stellar interior from stellar structure models. Our stellar structure models for the red giants considered here are run using version 7623 of MESA (Paxton et al. 2011, 2013, 2015, 2018, 2019). Models were run without rotation, overshooting, diffusion, or mass loss. Convection was treated according to the Cox & Giuli (1968) mixing length prescription. Opacities were generated from OPAL (Iglesias & Rogers 1993, 1996) using Grevesse & Sauval (1998) solar abundances, with C/O enriched abundance mixtures assumed for helium burning. The parameter file used to compute our models is provided in Appendix A. We consider the evolution of red giants at two different mixing length parameters and a range of metallicities to gain a coarse understanding as a function of mass, metallicity, and mixing length of how the adiabatic assumption leads to errors in $f_{\Delta\nu}$ and therefore asteroseismic radius and mass. The Hertzsprung-Russell diagram of our models are shown in Figure 1.

2.2. GYRE non-adiabatic treatment

We use GYRE to compute asteroseismic frequencies for our stellar models. GYRE may treat the stellar pulsation equations with or without the adiabatic approximation, and does so by linearizing the energy transport equation, which we briefly review here.

We may write the left-hand side of Equation 2 as a balance of sources and sinks, i.e., a balance between energy generation per unit mass, ϵ , and the energy flux, \vec{F} :

$$\frac{dq}{dt} = \epsilon - \frac{1}{\rho} \nabla \cdot \vec{F}. \quad (9)$$

In the above, \vec{F} includes both convective and radiative fluxes.

GYRE linearizes the heat equation in Equation 9 and therefore may take into account non-adiabatic effects in the pulsation equations. It does so according to:

$$\frac{\partial \delta q}{\partial t} = \delta \epsilon - \frac{1}{\rho} \nabla \cdot (\vec{F}_{\text{rad}}' + \xi [\nabla \cdot \vec{F}_{\text{rad}}]), \quad (10)$$

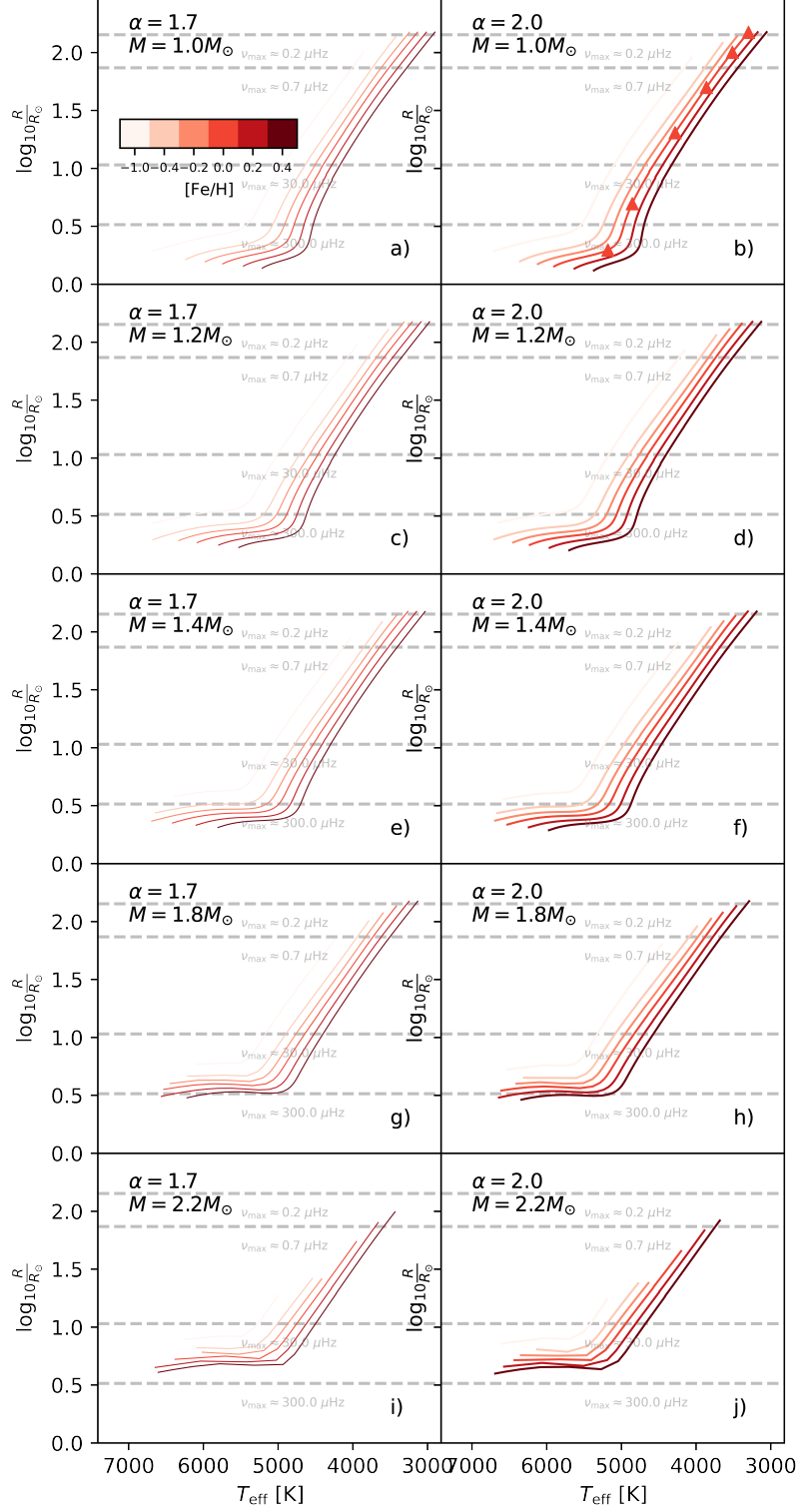


Figure 1: Stellar evolution tracks up to the RGB tip for all of the models considered here, where luminosity increases with increasing radius. The RGB bump is not included by requiring that the radii along the giant branch are monotonically increasing, nor are models with an effective temperature too hot to support solar-like oscillations. Each panel represents a different mass/mixing length parameter combination, while each track has a color corresponding to its metallicity according to the color bar. The triangles mark solar-mass, solar-metallicity, $\alpha = 2.0$ models shown in Fig. 5.

where δ indicates a Lagrangian perturbation and a prime indicates an Eulerian perturbation. Here, ξ is the Eulerian perturbation of the position and \vec{F}_{rad} is the radiative flux. The radiative flux is perturbed according to the diffusion approximation. The convective flux does not enter into the above linearization because GYRE operates under the frozen convection approximation, where the convective flux is not perturbed (meaning there is no coupling between convection and pulsation).

The parameter file used to compute stellar pulsation frequencies with GYRE is provided in Appendix B.

2.3. Calculating adiabatic and non-adiabatic $f_{\Delta\nu}$

The $f_{\Delta\nu}$ values are determined by first computing a model-observed $\Delta\nu$ ($\Delta\nu_{\text{obs}}$), according to the procedure described in White et al. (2011), wherein the differences between radial frequencies are fitted with a least-squares approach and a weighting that is designed to mimic observational methods of determining $\Delta\nu$. In detail, the weights are assigned according to a Gaussian centered on ν_{max} , and with a ν_{max} -dependent standard deviation, σ taken from (Zinn et al. 2019b): $\sigma = 1.05 \ln \nu_{\text{max}} - 1.91$. We compute $\Delta\nu_{\text{obs}}$ both under the adiabatic approximation ($\Delta\nu_{\text{obs,ad}}$) and in the non-adiabatic treatment ($\Delta\nu_{\text{obs,nonad}}$).

We visually demonstrate the method for determining $\Delta\nu$ in Figure 2. The weights for each of the frequency differences that go into $\Delta\nu$ are indicated by the Gaussian in Fig. 2a. This Gaussian represents roughly the relative amplitude of the modes that would be measurable in surface brightness variation measurements. Note that the width of the Gaussian increases with ν_{max} , encompassing more of the modes of the $R \approx 2R_{\odot}$ model than of the $R \approx 150R_{\odot}$ model, which only has a few modes that would be measurable. We also see in this panel that the difference between the adiabatic and non-adiabatic frequencies (dashed versus dotted vertical lines) increases with increasing frequency. This is due to the known behavior of higher-order radial modes to be more localized to the surface than lower-order radial modes: as we show in §3.3, the outer layers of evolved stars are the most non-adiabatic, and so the adiabatic assumption is increasingly worse not only for evolved stars, but also for higher-order radial modes. We see the effect of this on the $\Delta\nu$ measurement in Fig. 2b, which shows the difference between successive $\ell = 0$ frequencies. The final $\Delta\nu_{\text{obs,ad}}$ and $\Delta\nu_{\text{obs,nonad}}$ are the Gaussian-weighted averages of the respective curves shown here. The more evolved star shows significant departures between the adiabatic and non-adiabatic frequency differences with increasing frequency. Note that the y-axis here is nor-

malized to the non-adiabatic $\Delta\nu$, and so the effect is such that $\Delta\nu_{\text{nonad}}$ is smaller than $\Delta\nu_{\text{ad}}$.

The effect of non-adiabaticity on $\Delta\nu$ could plausibly be a function of bulk stellar properties (e.g., metallicity or mass). We therefore generalize this difference between $\Delta\nu_{\text{nonad}}$ and $\Delta\nu_{\text{ad}}$ across mass, metallicity, and mixing length, and as a function of radius in §3.

3. RESULTS AND DISCUSSION

3.1. The adiabatic error as a function of stellar mass, metallicity, and mixing length

In Figure 3 is shown the error that would be induced in the asteroseismic radii via a $f_{\Delta\nu}$ computed under the adiabatic approximation (called the adiabatic error in the following discussion). The error here is shown in percent, where a positive value would mean that a non-adiabatic $f_{\Delta\nu}$ reduces the asteroseismic radius. The effect is as large as 10% near the tip of the giant branch, and is less than $\approx 2\%$ for stars with $R \lesssim 30R_{\odot}$.

Figure 3 shows a modest metallicity-dependent error, and a few percent difference in the adiabatic error between the $M = 1M_{\odot}$ and $M = 1.8M_{\odot}$ models for models above $R \approx 100R_{\odot}$; the $M = 2.2M_{\odot}$ model does not go as high up the giant branch as the other models, but is consistent with the others up to $R \approx 100R_{\odot}$. There also does not appear to be a significant difference between the error between the two mixing length parameters considered.

The fractional error induced in the asteroseismic radius scaling relation (Eq. 7) by calculating $f_{\Delta\nu} \equiv \Delta\nu / \Delta\nu_{\text{obs}}$ in the adiabatic approximation is given solely by the ratio of $\Delta\nu_{\text{obs,ad}}^2 / \Delta\nu_{\text{obs,nonad}}^2$ (see Equation 7), which we abbreviate as $\Delta\nu_{\text{ad}}^2 / \Delta\nu_{\text{nonad}}^2$ in what follows.

3.2. Impact of the adiabatic error on the asteroseismic radius scale

Having established that the adiabatic error will tend to inflate asteroseismic radii if not corrected, we now apply non-adiabatic corrections to the asteroseismic radius scale and compare the resulting radii with independent radii from Gaia. The asteroseismic data we use for this are from APOKASC-3 (M. H. Pinsonneault et al., in preparation), with the Gaia EDR3 (Gaia Collaboration et al. 2021) radii computed according to Zinn et al. (2017) and Zinn (2021), with Gaia parallax corrections from Lindegren et al. (2021a) and Zinn (2021).¹

¹ The comparison here is not sensitive to the Gaia parallax zero-point, after corrections from (Lindegren et al. 2021a) are applied to the parallaxes. The Gaia parallax zero-point uncertainty from Zinn (2021) is negligible in its effect on the Gaia radii and cannot explain the discrepancy, which has also been noted by Kallinger et al. (2018) for stars with $R \sim 30R_{\odot}$.

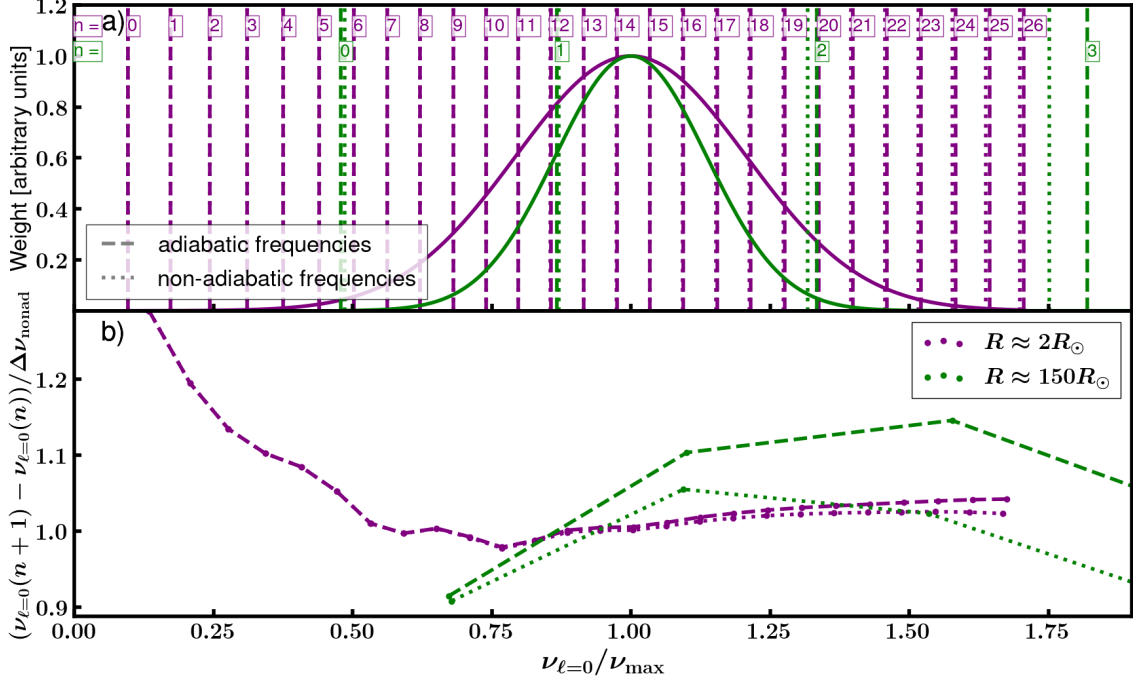


Figure 2: a) The modelled $\ell = 0$ frequencies for a solar-mass, solar-metallicity, $\alpha = 2.0$ star at $R \approx 2R_\odot$ (purple vertical lines) and $R \approx 150R_\odot$ (green vertical lines) computed with and without the adiabatic assumption (solid and dashed lines, respectively), normalized by ν_{\max} . The radial order for each frequency is listed as n . The weighting scheme used to compute an average difference between successive modes is given by a Gaussian centered around ν_{\max} , the width of which depends on ν_{\max} . b) The difference between frequencies of adjacent radial order, n , as a function of frequency. The $R \approx 150R_\odot$ star has many fewer modes around ν_{\max} (number of vertical lines within the Gaussian in panel a) and $\Delta\nu$ is affected much more by the adiabatic assumption (difference between green curves in panel b).

The parallax statistical uncertainties are re-calibrated according to El-Badry et al. (2021). The Gaia radius calculation proceeds according to the Stefan-Boltzmann law, where a luminosity is computed from a K_s bolometric correction from (González Hernández & Bonifacio 2009) and Gaia parallax (Gaia Collaboration et al. 2021; Lindegren et al. 2021b), as well as extinctions from Green et al. (2019), as implemented in `mwdust`² (Bovy et al. 2016). The uncertainties on the extinctions are assumed to be 0.08mag, and effective temperatures are adopted from APOGEE DR16 (Ahumada et al. 2020). $f_{\Delta\nu}$ from Sharma et al. (2016) and Sharma & Stello (2016)³ are computed using APOGEE effective temperatures and metallicities; evolutionary state classifications from M. H. Pinsonneault et al., in preparation; and asteroseismic surface gravity from Equation 4. The metallicities are corrected for non-solar abundances in

the Salaris et al. (1993) approximation using APOGEE [α/M].

We first show in Figure 4 the disagreement between Gaia EDR3 radii and asteroseismic radii computed using no $\Delta\nu$ corrections ($f_{\Delta\nu} = 1$ in Eq. 6; grey error bars). Asteroseismic radii computed with $f_{\Delta\nu} = 1$ are inflated compared to Gaia radii at all $R > 4R_\odot$, with a $\approx 10\%$ error near the tip of the giant branch.

Looking to the purple error bars, we see that theoretical $f_{\Delta\nu}$ from Sharma et al. (2016) and Sharma & Stello (2016) calculated in the adiabatic approximation reduce the disagreement until $R \approx 30R_\odot$ (purple error bars). This is the first indication that the agreement between adiabatic $\Delta\nu$ -corrected asteroseismic radii and independent Gaia radii is very good up to a radius of $\approx 50R_\odot$: the median agreement for stars with $10R_\odot \leq R < 30R_\odot$ and for $30R_\odot \leq R < 50R_\odot$ is within the systematic uncertainties of the asteroseismic radius scale ($\approx 2\%$; Zinn

² <https://github.com/jobovy/mwdust>

³ The `asfgrid` code is publicly available at <http://www.physics.usyd.edu.au/k2gap/Asfgrid/>

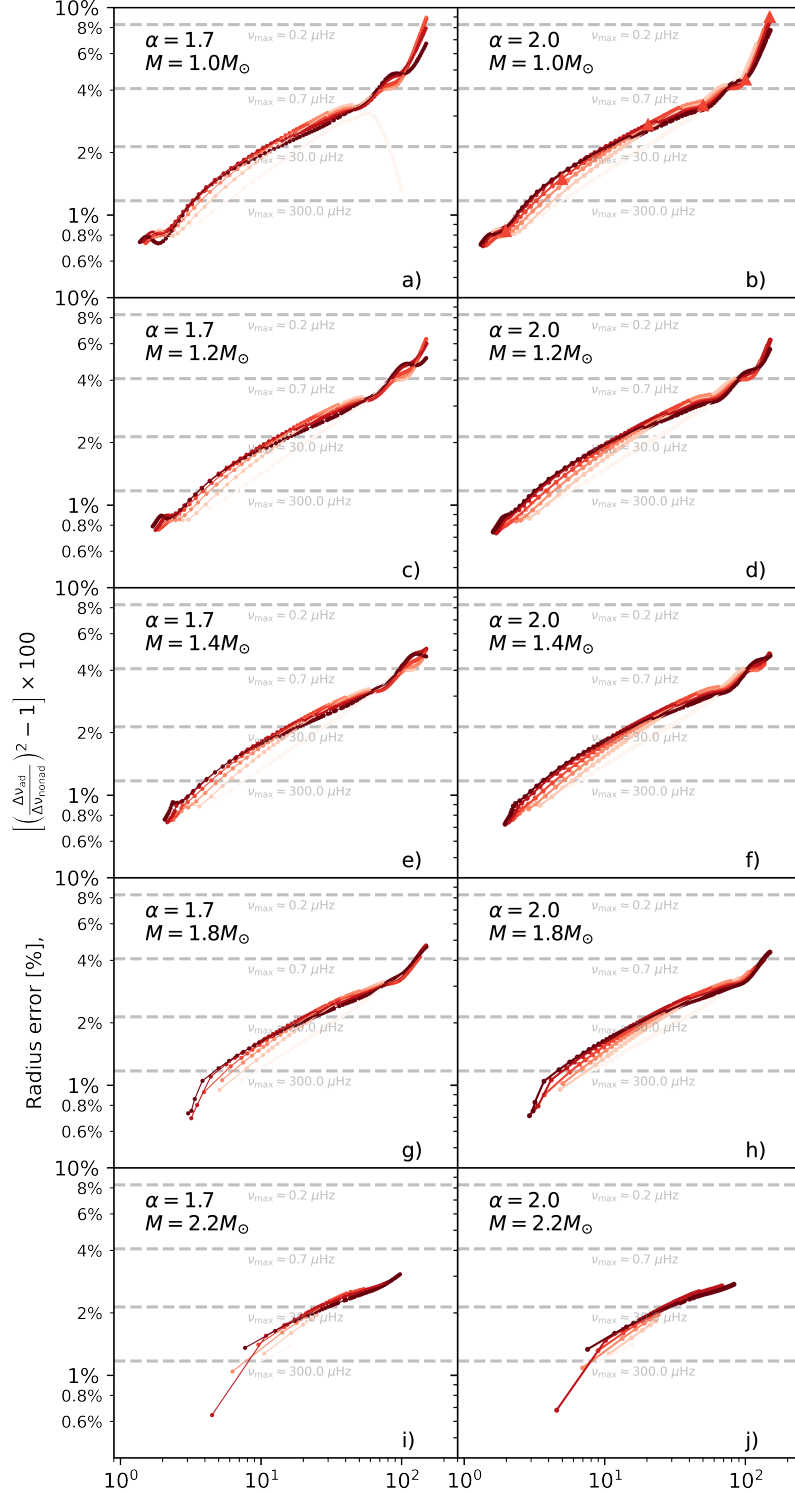


Figure 3: The expected error from using the asteroseismic radius scaling relation (Equation 7) with theoretical corrections to observed $f_{\Delta\nu}$ in the adiabatic approximation (what we call the ‘adiabatic error’), in percent. Each point represents the error for stars of mass ($1M_{\odot}$, $1.2M_{\odot}$, $1.4M_{\odot}$, $1.8M_{\odot}$, $2.2M_{\odot}$), metallicities (-1, -0.4, -0.2, 0.0, 0.2, 0.4), and mixing length parameters (1.7, 2.0) at various stages of evolution along the first-ascent giant branch. The RGB bump is excluded, as are models with $R > 150R_{\odot}$. Positive errors indicate that the asteroseismic radius is too large, which is consistent with the tension compared to independent Gaia radii shown in Figure 4. Each panel represents a different mass/mixing length parameter combination, while each track has a color corresponding to its metallicity according to the color bar of Fig. 1. The triangles mark solar-mass, solar-metallicity, $\alpha = 2.0$ models shown in Fig. 5. Horizontal dashed lines give the approximate adiabatic errors for the solar-mass, solar-metallicity, $\alpha = 2.0$ models at various ν_{\max} values, for reference (in detail, ν_{\max} depends on mass, metallicity, and α).

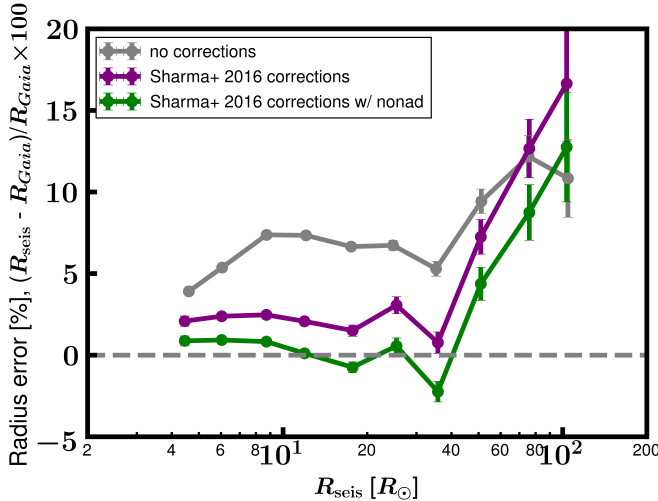


Figure 4: Fractional difference of asteroseismic and Gaia radii in the regime usually probed by asteroseismic studies ($R \lesssim 30R_{\odot}$) and in the luminous giant regime ($R \gtrsim 30R_{\odot}$) for stars with $1 < M_{\odot} < 2.2$ and $-2 < [\text{Fe}/\text{H}] < 0.4$. The binned medians and uncertainty on the medians of the fractional radius difference for raw asteroseismic scaling relation radii (Equation 7, with $f_{\Delta\nu} = f_{\nu_{\max}} = 1$) are shown in grey error bars. If the asteroseismic radii agreed with Gaia, the data would follow the horizontal dashed line. The improvement from correcting $\Delta\nu$ according to theoretical corrections from Sharma et al. (2016) in the adiabatic regime are shown as purple error bars (Equation 7, with $f_{\Delta\nu} \neq 1, f_{\nu_{\max}} = 1$); though the agreement is improved at smaller radii, at radii $R \gtrsim 30R_{\odot}$, the discrepancy persists and becomes worse than uncorrected asteroseismic radii. Correcting $f_{\Delta\nu}$ for non-adiabatic effects results in better agreement at large radii (green error bars). See text for details.

et al. 2019a).⁴ Previous indications from APOKASC-2 data (Pinsonneault et al. 2018) indicated the agreement for stars with $10R_{\odot} \leq R < 30R_{\odot}$ was $1.9\% \pm 0.6\%$ and for stars with $R > 30R_{\odot}$ was $8.7\% \pm 0.9\%$ (Zinn et al. 2019a), in the sense that asteroseismic radii were too large. This indicates a significant improvement in agreement with APOKASC-3 compared to APOKASC-2 for stars with $R > 30R_{\odot}$. This improvement may be due to

⁴ The absolute level of agreement in Figure 4 is uncertain at the 2% level, and depends on the temperature scale, bolometric correction choices, and choices in the normalization of the scaling relations ($\nu_{\max,\odot}$ and $\Delta\nu_{\odot}$ in Eq. 7; Zinn et al. 2019a). That non-adiabatic corrections improve agreement in the luminous giant regime — where the disagreement between adiabatic asteroseismology and Gaia is at the 10% level — holds true despite small shifts in these scales.

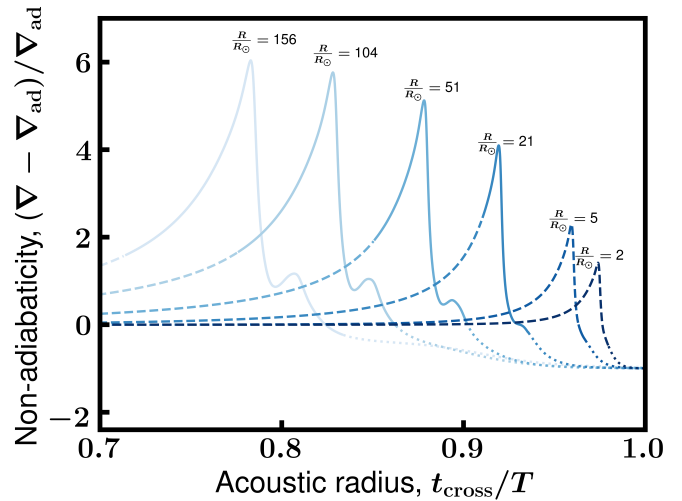


Figure 5: The fractional difference in the actual average temperature gradient, ∇ , from the adiabatic case, ∇_{ad} , as a function of the acoustic radius (Equation 11) for solar-mass, solar-metallicity, $\alpha = 2.0$ models at stellar radii of $\approx 2R_{\odot}$, $5R_{\odot}$, $20R_{\odot}$, $30R_{\odot}$, $100R_{\odot}$, and $160R_{\odot}$, from right to left. An acoustic radius of 0 corresponds to the stellar center, and one of unity corresponds to the stellar surface. Dotted curves correspond to where MESA attaches an Eddington atmosphere. More evolved first-ascent red giant branch stars have envelopes that are more strongly non-adiabatic and are non-adiabatic for a larger fraction of the acoustic cavity than those of less-evolved first-ascent red giant branch stars, which may be partially responsible for a breakdown in the (adiabatic) asteroseismic scaling relations among giants with $R \gtrsim 50R_{\odot}$. In particular, that more of the non-adiabatic region is in the regime where the thermal and sound crossing timescales have a ratio of $t_{\text{th}}/t_{\text{cross}} < 1$ (solid curves), indicates that their theoretical asteroseismic frequencies should not be computed in the adiabatic approximation. The acoustic radius of both the peak non-adiabaticity and the top of the convection zone ($\nabla - \nabla_{\text{ad}} = 0$) move in step with each other, suggesting a relationship between the non-adiabatic region expansion with increasing stellar radius and convection physics.

two changes implemented in APOKASC-3 compared to APOKASC-2: 1) the APOKASC-3 analysis used data that were optimized for high-luminosity stars; and 2) the APOKASC-3 analysis used improved outlier rejection when combining ν_{\max} and $\Delta\nu$ results from different pipelines to yield the consensus ν_{\max} and $\Delta\nu$ values. Ultimately, whatever shortcomings there may be in the asteroseismic $\Delta\nu$ scaling relation would therefore seem to affect the highest luminosity stars with $R \gtrsim 50R_{\odot}$,

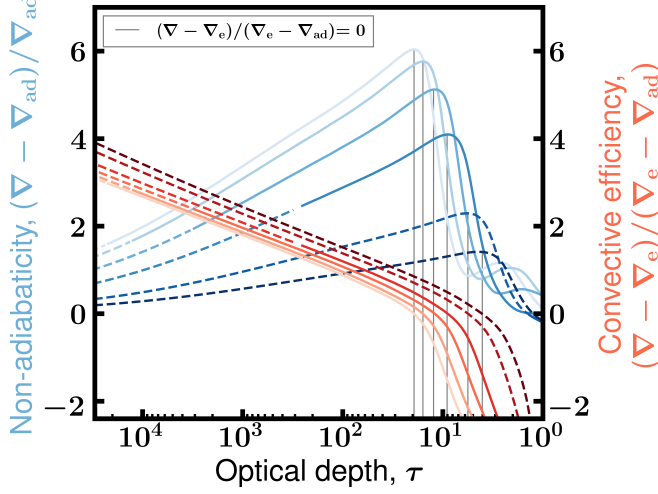


Figure 6: The fractional difference in the temperature gradient from the adiabatic case (left axis) and the efficiency of convection (right axis), as a function of optical depth for solar-mass, solar-metallicity, $\alpha = 2.0$ models at stellar radii of $\approx 2R_\odot$, $5R_\odot$, $20R_\odot$, $50R_\odot$, $100R_\odot$, and $160R_\odot$, from right to left. The red and blue curves of the same hue correspond to the same model. Convective efficiency less than 0 means that radiation dominates the energy transport, even if the region is still convective. Solid, dashed, and dotted parts of the non-adiabaticity curves are the same as in Fig. 5. Peaks in the non-adiabaticity correspond well to where the convective efficiency equals 0 (solid vertical lines).

leaving less evolved stars with scaling relation radii accurate to at least 2%.

Nevertheless, the disagreement sharply increases to 10% for $\Delta\nu$ -corrected radii for stars with $R \approx 50R_\odot$, and the corrections actually aggravate the uncorrected radius error at larger radii to become $\approx 15\%$ for $R \approx 100R_\odot$. This disagreement can be partially mitigated, however, by applying non-adiabatic corrections, which is shown by the green error bars. In this case, the $\Delta\nu$ corrected according to $f_{\Delta\nu}$ from Sharma et al. (2016) are multiplied by $\Delta\nu_{\text{obs,nonad}}/\Delta\nu_{\text{obs,ad}}$ from our models, using linear interpolation as a function of metallicity, mass, and ν_{max} . This correction is meant to take into account the increase in $\Delta\nu$ we find using non-adiabatic pulsation frequencies (e.g., Figs. 2 & 3).

It should also be noted that the inflated asteroseismic radius scale implies an inflated asteroseismic mass scale, as well: both Equation 3 & 4 depend on $f_{\Delta\nu}$ in the same sense. The mass dependence on $f_{\Delta\nu}$ is even stronger than that of radius, and so, fractionally, the inferred inflation of the asteroseismic mass scale is larger than

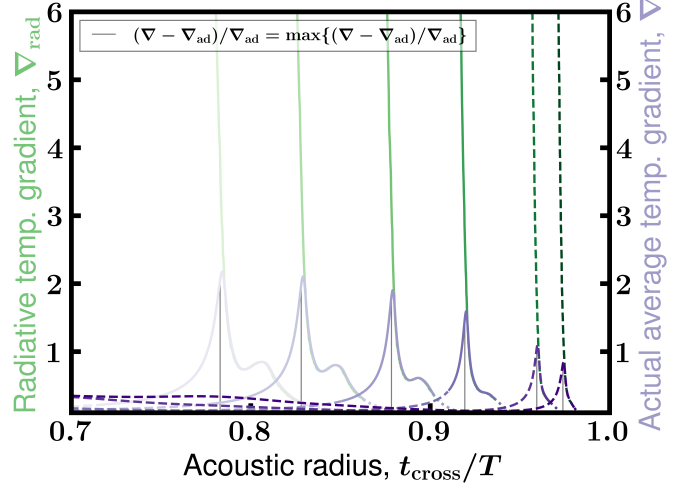


Figure 7: The radiative thermal gradient (left axis) and the actual average thermal gradient (right axis), as a function of acoustic radius for solar-mass, solar-metallicity, $\alpha = 2.0$ models at stellar radii of $\approx 2R_\odot$, $5R_\odot$, $20R_\odot$, $50R_\odot$, $100R_\odot$, and $160R_\odot$, from right to left. The purple and green curves of the same hue correspond to the same model. The peak of the non-adiabaticity shown in the blue curves of Figs. 5 & 6 is indicated by the vertical lines. Solid, dashed, and dotted parts of the non-adiabaticity curves are the same as in Fig. 5. The convective efficiency of the models decreases from small to large acoustic radius (from stellar interior to exterior), and, as it does, the actual average thermal gradient approaches the radiative thermal gradient, which describes the thermal gradient in the limit that all of the energy is transported via radiation. $\nabla = \nabla_{\text{rad}}$ corresponds to the maximum non-adiabaticity in each model, which then decreases, since ∇ continues to track the radiative thermal gradient, which decreases with increasing acoustic radius. A small increase in ∇ and ∇_{rad} exterior to the non-adiabaticity maximum corresponds to the hydrogen partial ionization zone.

the observed asteroseismic radius scale inflation seen in Figure 4.

3.3. Physical origins of non-adiabaticity in luminous giants

The very good agreement in Gaia and asteroseismic radius for the less luminous stars prompts us to consider the physical reasons behind the dramatic onset of asteroseismic radius inflation seen in Figure 4.

We show in Figure 5 the fractional difference between the actual temperature gradient, $\nabla \equiv \frac{d \ln T}{d \ln P}$, and the temperature gradient in the adiabatic approximation, ∇_{ad} as a function of the acoustic radius. Given the local sound crossing timescale, $t_{\text{cross}}(r) \equiv \frac{dr}{c(r)}$, where $c(r)$ is

the local sound speed at radius, r , we define the acoustic radius to be

$$t_{\text{cross}}/T \equiv \int_r^R \frac{dr}{c(r)} / \int_0^R \frac{dr}{c(r)} \quad (11)$$

$$\equiv \int dr \frac{\rho(r)}{\Gamma_1(r)P(r)} / \int_0^R \frac{dr}{c(r)}. \quad (12)$$

Here, Γ_1 is the local adiabatic exponent, ρ is the local gas density, P is the local pressure, and the integration limits are such that the acoustic radius increases from 0 at the stellar center to 1 at the stellar surface.

We can see in Figure 5 that the more evolved the first-ascent RGB star, the longer time a mode will travel through a non-adiabatic region. This observation is only important, however, if the heat exchange occurs on a timescale that an asteroseismic mode experiences. The two relevant timescales are the local thermal timescale and the local sound crossing timescale. The local sound crossing timescale is given by Equation 11. The local thermal timescale is the time taken to transport the energy of a shell of mass $dm = 4\pi r^2 dr \rho(r)$, given the local luminosity, $\ell(r)$. Given the internal energy per mass of a monatomic gas, $u = 3/2 \frac{RT}{\mu}$ and the ideal gas law $P = \frac{R\rho T}{\mu}$, we have that the local thermal timescale is

$$t_{\text{th}} \equiv dm(r)u(r)/\ell(r) \quad (13)$$

$$t_{\text{th}} = 4\pi r^2 dr \rho(r) 3/2 \frac{RT}{\mu} / \ell(r) \quad (14)$$

$$= 6\pi r^2 dr P(r) / \ell(r), \quad (15)$$

so the ratio of the local thermal timescale to the local sound crossing timescale is

$$t_{\text{th}}(r)/t_{\text{cross}}(r) = 6\pi r^2 P(r)c(r)/\ell(r). \quad (16)$$

Solid curves in Figure 5 indicate regions where this ratio is below unity, corresponding to where the thermal timescale is shorter than the time taken for the mode to travel the region. This means that the mode will be sensitive to local heat exchange. To the extent that these regions correspond to non-adiabatic regions in the star, the assumption of adiabaticity will be invalid for the linearized energy transport equation (Equation 2). We see that the more evolved, larger RGB stars have a larger fraction of their acoustic radius in this regime (solid curves where the non-adiabaticity is non-zero in Fig. 5).

Looking at Figure 5, we see that for less evolved stars (smaller radii), the non-adiabaticity peaks at smaller acoustic radii; this peak occurs at larger acoustic radii for more evolved stars (larger radii). At the same time, the top of the convection zone (where $\nabla - \nabla_{\text{ad}} = 0$)

similarly moves deeper into the star with increasing radius. This connection between a convective property of the models (the extent of the convection zone) and the location of peak non-adiabaticity motivates investigating the convection properties of the giants as causing non-adiabaticity.

We start by considering the convective efficiency, following Cox & Giuli (1968):

$$\Gamma \equiv \frac{\nabla - \nabla_e}{\nabla_e - \nabla_{\text{ad}}}, \quad (17)$$

where ∇_{ad} is the adiabatic thermal gradient, ∇ is the actual average thermal gradient, and ∇_e is the thermal gradient of a convective element. The above assumes the convective element produces no energy, and only loses it to its environment through radiation. In the limit of efficient convection (large Γ), the fraction of energy carried by convection will approach unity, as long as the radiative thermal gradient is sufficiently larger than the adiabatic thermal gradient. In the limit of inefficient convection ($\Gamma \leq 0$), the fraction of energy carried by convection goes to zero as the actual average thermal gradient and the convective element thermal gradient both approach the radiative thermal gradient.

The convective efficiency behavior shown in red hues in Figure 6 explains qualitatively the behavior of the non-adiabaticity shown in blue hues in Figure 6. Using optical depth rather than acoustic radius as our radial coordinate emphasizes that the evolved stars may have non-adiabatic regions relatively deep in acoustic radius space, but they occur at relatively small optical depth because more evolved stars are larger but more diffuse than less evolved stars. At large optical depth, the convective efficiency is large, and the actual average thermal gradient is equal to the adiabatic thermal gradient, which is at all times less than unity and nearly constant. As the optical depth decreases, convective efficiency decreases, such that convective elements lose more and more energy to radiation. Less energy is carried via convection and more by radiation, so the actual average thermal gradient approaches the radiative thermal gradient, which is much larger than the adiabatic thermal gradient. We see this transition in Figure 7. Here, we show the actual average thermal gradient (purple curves) and the radiative thermal gradient (green curves). The actual average thermal gradient, ∇ , increases with increasing acoustic radius because the convective efficiency is decreasing (red curves in Fig. 6), until the point at which the convective efficiency becomes zero, which corresponds to $\nabla = \nabla_{\text{rad}}$ (intersection of the purple and green curves in Fig. 7). This results in a maximum in the non-adiabaticity (indicated by the ver-

tical lines) because $\nabla = \nabla_{\text{rad}}$ from here to the surface of the star (green curves and purple curves coincide), and ∇_{rad} is decreasing outward to the stellar surface.⁵ The non-adiabaticity therefore peaks at very low convective efficiencies ($\Gamma \approx 0$), where both the actual average thermal gradient and the convective element thermal gradient both equal the radiative thermal gradient. The actual average thermal gradient will continue to track the radiative thermal gradient, which continually decreases due primarily to the decreasing opacity while the adiabatic gradient remains constant; the non-adiabaticity thus decreases with decreasing optical depth beyond the point of maximum non-adiabaticity.

Ultimately, the opacity is the main driver of this behavior: in evolved stars, the opacity is lower for a larger part of the convective envelope than with less evolved stars, given the low envelope temperatures. This leads to a decrease in convective efficiency due to increased radiative losses (being proportional to $1/\kappa$), and therefore the actual average thermal gradient approaches the radiative thermal gradient well into the convective region. The same behavior happens in less evolved stars, but at shallower depths. The amplitude and extent of the non-adiabatic region differ between less and more evolved stars because $\Gamma = 0$ occurs at lower optical depth for less evolved stars (Fig. 6), which also corresponds to a smaller radiative thermal gradient. This means less evolved stars have a smaller ∇_{rad} than the actual thermal gradient needs to reach, and therefore a smaller amplitude of the peak non-adiabaticity. Since the slope of the convective efficiency with optical depth is the same no matter how evolved the stars is (Fig. 6), the physical extent of the non-adiabatic region is also smaller for less evolved stars, since the actual thermal gradient needs to climb to a smaller value at the same rate as a more evolved star.

3.4. Luminous giant asteroseismic scaling relation errors: $f_{\nu_{\text{max}}}$ or $f_{\Delta\nu}$?

The adiabatic error in $f_{\Delta\nu}$ of $\approx 4\%$ for stars with $R \approx 100R_{\odot}$ we find (Fig. 3) still leaves a $\approx 5\% - 10\%$ margin of unexplained systematic difference in asteroseismic radii for stars with $R \gtrsim 50R_{\odot}$ compared to Gaia radii (green curve in Fig. 4). The adiabatic error we have demonstrated is thermodynamic in nature, but other contributions to an error in $f_{\Delta\nu}$ could very well arise due to structural problems in the model.

⁵ The decrease outward is not monotonic, however: there is a small increase in ∇_{rad} due to the partial ionization zone of hydrogen (secondary bumps in ∇ seen in Fig. 7 at larger acoustic radius than the primary peaks).

For instance, as we have shown, large parts of the acoustic cavity exhibit low convective efficiency (Fig 6), and would therefore require a different treatment of convection than mixing length theory can provide (which assumes no radiative losses of a convective element). Existing work has shown that 1D mixing length theory yields meaningfully different stellar structure in the outer layers of a star compared to outer layer structures from 3D treatments of convection (e.g., Trampedach et al. 2017; Jørgensen et al. 2019; Mosumgaard et al. 2020). The resulting effect on asteroseismic frequencies — the so-called structural surface effect — is in addition to a so-called modal surface effect, which is an error resulting from neglecting the coupling of convective motions to asteroseismic modes, which requires an in-depth treatment of the turbulent and convective physics in the convective envelope (e.g., Balmforth 1992; Xiong et al. 1997; Grigahcène et al. 2005). Structural surface effects have been considered for the red giant case (e.g., Trampedach et al. 2017) as have modal surface effects (e.g., Xiong 2021), but both effects have not yet been considered together. To date, the combination of these effects on asteroseismic frequencies, to our knowledge, has only been studied in the solar case, which yields excellent agreement with observed frequencies (Houdek et al. 2017).

There has also been an effort to correct for these surface effects empirically, via so-called surface corrections. Surface corrections are used in grid-based asteroseismic modelling wherein observed individual frequencies are fit using models to derive stellar parameters (see, e.g., Serenelli et al. 2017, and references therein), which is in contrast to the scaling relations of interest to us here. Surface corrections take the form of power laws as a function of frequency, the parameters of which are fit on a star-by-star basis to bring modelled and observed frequencies into the best possible agreement. Surface corrections of $\sim 1\%$ are required to bring modelled and observed frequencies into alignment among main sequence stars (Kjeldsen et al. 2008) and up to 2% in subgiants (Ball & Gizon 2017). Supporting findings from Sonoi et al. (2015), Li et al. (2018) find typical surface corrections of order 0.3% among giants more evolved than $R \sim 10R_{\odot}$. Surface corrections have not been quantified for more evolved giants, to our knowledge, but because lower giant branch corrections appear smaller than those for the main sequence, they may be similarly small on the upper giant branch.

Another structural issue that may contribute to errors in $f_{\Delta\nu}$ is the assumption of a 1D, plane-parallel, Eddington atmosphere, which becomes increasingly inaccurate to describe the $T_{\text{eff}} - \tau$ relation in the atmosphere of the

star. Indeed, we see that the atmosphere (dotted curves in Fig. 5) occupies more and more of a star’s acoustic radius with increasing stellar radius. The result is that the atmospheric temperature and opacity structure of the atmosphere would increasingly impact the mode structure and frequencies for more evolved stars.

Furthermore, there are several reasons to believe that systematics in ν_{\max} are responsible for a non-negligible part of the luminous giant asteroseismic radius problem. First, it is plausible that there are measurement systematics in ν_{\max} that are separate from any theoretical problems in the scaling relations themselves. This is because, for luminous giants, there are only a handful of modes that are visible (e.g., $R \approx 150R_{\odot}$ case in Fig. 2), which invalidates the approximation most asteroseismic pipelines make to measure ν_{\max} (viz., the modes can be modelled with a Gaussian in frequency space). There is also a possibility that the granulation among these high-luminosity giants behaves differently than on the lower giant branch. Choices in the model for the contribution of granulation to observed power spectra of solar-like oscillators can affect ν_{\max} measurements at the percent level in lower giant branch stars (Kallinger et al. 2014), and this may be aggravated at low frequency due to potential changes in the underlying ‘true’ model of granulation in these luminous stars and/or due to changes in how the models fit in the regime where there are relatively few data points to constrain the granulation parameters.

Apart from measurement issues implicated in luminous giant ν_{\max} , there could be problems in the ν_{\max} scaling relation itself that would cause a $f_{\nu_{\max}} \neq 1$. Viani et al. (2017), for instance, propose a metallicity-dependent term to the ν_{\max} scaling relation, based on the logic that the ν_{\max} scaling relation is a statement about the pressure scale height and the sound speed at the surface of a star, which depends on the mean molecular weight. More detailed theoretical motivations for $f_{\nu_{\max}}$ that are analogous to theoretically-computed $f_{\Delta\nu}$ will need to await improved modelling of the excitation and damping effects in models (e.g., Zhou et al. 2020).

3.5. Comparison to other work

Bulgen et al. (2019) computed surface correction effects due to the adiabaticity assumption for low-luminosity first-ascent red giants with mass $1.05 - 1.4M_{\odot}$ and radius $2.47 - 2.77R_{\odot}$. Their analysis differs from ours in the crucial aspect that theirs was an inversion exercise, using individual mode frequencies to derive a stellar density, which was then compared to the truth. Their Fig. 10 shows that the adiabatic frequency approximation is a negligible error contribution, when con-

sidering $n=1-20$ modes. Ultimately, our results are not comparable to theirs, given we are interested in errors introduced in scaling relations, not when using inversion techniques.

The onset of the thermal timescale becoming shorter than the sound crossing timescale (solid curves in Fig. 6) is also consistent with a 3D simulation of the stellar envelope of a $2M_{\odot}$, solar metallicity red giant branch star with $\log g = 1$ from Ludwig & Kučinskas (2012). Our 1D MESA model of a $1M_{\odot}$ red giant branch star with $50R_{\odot}$ model has the same surface gravity as their model. As shown in Figure 6, its thermal–sound crossing timescale transition occurs at $\tau \sim 3000$, and in the Ludwig & Kučinskas (2012) 3D model this transition occurs at $\tau \sim 1000$. Ludwig & Kučinskas (2012) conclude that the structure from their 3D simulation cannot be described using a stellar structure from 1D mixing length theory, which further motivates investigating the impact of structural errors in the convective envelope on $f_{\Delta\nu}$.

Regarding the small metallicity dependence of the adiabatic error in Figure 3, Epstein et al. (2014) found that scaling relation masses, corrected for $f_{\Delta\nu}$, of metal-poor ($[\text{Fe}/\text{H}] < 1$) stars are too massive by $11\% \pm 4\%$. Using a metallicity-dependent $\Delta\nu$ correction, Sharma et al. (2016) found metal-poor stars are too massive by only $4\% \pm 5\%$. This would imply a differential radius problem of order 6% (2 – 3% according to Sharma et al. 2016). We do not find evidence of this for our $[\text{Fe}/\text{H}] = -1$ models compared to other metallicities. In fact, the $[\text{Fe}/\text{H}] = -1$ model $f_{\Delta\nu}$ are consistently less affected by the adiabatic assumption than other metallicities, no matter the mass or mixing length parameter (lightest curves in Fig. 3).

4. CONCLUDING REMARKS

We find that a large fraction of the acoustic radius (up to 20%) is highly non-adiabatic, which has a significant impact on the model-dependent corrections to the $\Delta\nu$ component of the asteroseismic scaling relations. The adiabatic error is found to be no larger than a couple percent for stars with radii below $\approx 30R_{\odot}$. This is consistent with the percent-level bounds in asteroseismic radius accuracy set here and by previous work using independent constraints from Gaia (Zinn et al. 2019a). However, the adiabatic error we predict reaches 10% at the tip of the giant branch. Empirical constraints on the asteroseismic radius scale from fundamental Gaia radii (Fig. 4) indicate that asteroseismic radii have errors in excess of this level for stars with $R \gtrsim 50R_{\odot}$, which suggests additional sources of errors in the asteroseismic scaling relations. It is possible that not only the impact of non-adiabatic thermodynamics on the modes but also

the structural impact of incorrect convection treatment in these zones may be a contributor. We show that, indeed, the non-adiabatic regions of the stars coincide with inefficient convection, which mixing length theory does not adequately describe, and which would induce structural changes affecting mode propagation. It is also likely that the ν_{\max} component of the scaling relations is responsible for systematic errors in luminous giant asteroseismic radii. Unfortunately, theoretical predictions for ν_{\max} that might permit a $f_{\nu_{\max}}$ correction to observed ν_{\max} (in analogy with $f_{\Delta\nu}$), are not yet precise enough (Zhou et al. 2020) to quantify the ν_{\max} contribution to asteroseismic radius errors.

Boutique, grid-based modelling whereby masses and radii are inferred based on fitting individual modelled modes to individual observed modes (as opposed to reducing the mode spectrum to the summary metrics of ν_{\max} and $\Delta\nu$) may be a fruitful way to approach the models of these stars. The success of this approach would depend more sensitively on the surface correction,

however, which has not to date been studied among stars with $R > 30R_{\odot}$.

We conclude that the most prudent way forward for making use of scaling relations in the luminous giant regime is to calculate corrections to asteroseismic scaling relations, $f_{\Delta\nu}$, with a non-adiabatic treatment. This work has considered radius errors, but errors in $\Delta\nu$ and ν_{\max} will also impact asteroseismic masses, which are crucial data in Galactic archaeology and stellar physics studies (e.g., Miglio et al. 2013; Rendle et al. 2019; Sharma et al. 2019; Miglio et al. 2021). One may reduce the impact of unknown, outstanding errors in the mass asteroseismic scaling relations due to ν_{\max} by using external radius measurements from Gaia in combination with non-adiabatic $\Delta\nu$ to yield hybrid Gaia-asteroseismic masses. Furthermore, APOKASC-3 data indicate that stars with $R \lesssim 30R_{\odot}$ have radii that agree to Gaia within at least 2% (Fig. 4), which would allow for accurate asteroseismology of stars more luminous than typically analyzed in the literature.

APPENDIX

A. MESA INLIST

```

&kap
use_Type2_opacities = .true.
Zbase = 4.3d-2
/

&eos
/

&star_job
show_log_description_at_start = .false.
create_pre_main_sequence_model = .true.
save_model_when_terminate = .true.
save_model_filename = 'final.mod'
write_profile_when_terminate = .true.
filename_for_profile_when_terminate = 'final_profile.data'
/

&controls
use_dedt_form_of_energy_eqn = .true.
use_gold_tolerances = .true.
mesh_delta_coeff = 0.5
use_other_mesh_functions = .true.
x_ctrl(1) = 500
x_ctrl(2) = 0.02d0
x_ctrl(3) = 0d0
max_years_for_timestep = 1d6
varcontrol_target = 1d-3

```

```

max_timestep_factor = 2d0
delta_lgT_cntr_limit = 0.1
delta_lgRho_cntr_limit = 0.5
num_trace_history_values = 2
trace_history_value_name(1) = 'rel_E_err'
trace_history_value_name(2) = 'log_rel_run_E_err'
photosphere_r_upper_limit = 1.5d2
mixing_length_alpha = 1.7
initial_mass = 1.2
initial_z = 4.3d-2
write_pulse_data_with_profile = .true.
pulse_data_format = 'GYRE'
format_for_FGONG_data = '(1p,5(E16.9))'
add_center_point_to_pulse_data = .false.
atm_option = 'T_tau'
atm_T_tau_relation = 'Eddington'
atm_T_tau_opacity = 'varying'
initial_y = 0.28
cool_wind_RGB_scheme = ''
cool_wind_AGB_scheme = ''
RGB_to_AGB_wind_switch = 1d-4
Reimers_scaling_factor = 0.7d0
Blocker_scaling_factor = 0.7d0
cool_wind_full_on_T = 1d10
hot_wind_full_on_T = 1.1d10
hot_wind_scheme = ''
/
&pgstar
/

```

B. GYRE INLIST

```

&model
model_type = 'EVOL'
file = 'profile.data.GYRE'
file_format = 'MESA'
/
&constants
G_GRAVITY = 6.6740800000e-08
R_sun = 6.958e10
M_sun = 1.988435e33
/
&mode
l = 0
tag = 'radial'
/
&osc
outer_bound = 'VACUUM'
nonadiabatic = .TRUE.
tag_list = 'radial'

```

```

alpha_thm = 1
/
&rot
/
&num
diff_scheme = 'MAGNUS_GL2'
nad_search = 'MINMOD'
restrict_roots = .FALSE.
/
&scan
grid_type = 'LINEAR'
freq_min_units = 'NONE'
freq_max_units = 'NONE'
freq_min = 1.0
freq_max = 40.0
n_freq = 2000
tag_list = 'radial'
/
&grid
w_osc = 10
w_exp = 2
w_ctr = 10
/
&shoot_grid
/
&recon_grid
/
&ad_output
summary_file = 'profile.data.GYRE.gyre_ad.eigval.h5'
summary_file_format = 'HDF'
summary_item_list = 'M_star,R_star,L_star,l,n_pg,n_g,omega,freq,E,E_norm,E_p,E_g'
detail_template = 'profile.data.GYRE.gyre_ad.mode-%J.h5'
detail_file_format = 'HDF'
detail_item_list = 'M_star,R_star,L_star,m,rho,p,n,l,n_p,n_g,omega,freq,E,E_norm,W,x,V,As,U,c_1,Gamma_1,nab'
freq_units = 'UHZ'
/
&nad_output
summary_file = 'profile.data.GYRE.gyre_nad.eigval.h5'
summary_file_format = 'HDF'
summary_item_list = 'M_star,R_star,L_star,l,n_pg,n_g,omega,freq,E,E_norm,E_p,E_g'
detail_template = 'profile.data.GYRE.gyre_nad.mode-%J.h5'
detail_file_format = 'HDF'
detail_item_list = 'M_star,R_star,L_star,m,rho,p,n,l,n_p,n_g,omega,freq,E,E_norm,W,x,V,As,U,c_1,Gamma_1,nab'
freq_units = 'UHZ'
/

```

/

ACKNOWLEDGMENTS

We thank Richard Townsend for guidance in GYRE’s non-adiabatic capabilities. JCZ is supported by an NSF Astronomy and Astrophysics Postdoctoral Fellowship under award AST-2001869. JCZ and MHP acknowledge support from NASA grants 80NSSC18K0391 and NNX17AJ40G.

Funding for the Stellar Astrophysics Centre (SAC) is provided by The Danish National Research Foundation (Grant agreement no. DNRF106).

This publication makes use of data products from the Two Micron All Sky Survey, which is a joint project of the University of Massachusetts and the Infrared Processing and Analysis Center/California Institute of Technology, funded by the National Aeronautics and Space Administration and the National Science Foundation.

This work has made use of data from the European Space Agency (ESA) mission *Gaia* (<https://www.cosmos.esa.int/gaia>), processed by the *Gaia* Data Processing and Analysis Consortium (DPAC, <https://www.cosmos.esa.int/web/gaia/dpac/consortium>). Funding for the DPAC has been provided by national institutions, in particular the institutions participating in the *Gaia* Multilateral Agreement.

Funding for the Sloan Digital Sky Survey IV has been provided by the Alfred P. Sloan Foundation, the U.S. Department of Energy Office of Science, and the Participating Institutions. SDSS-IV acknowledges support and resources from the Center for High-Performance Computing at the University of Utah. The SDSS web site is www.sdss.org.

Software: asfgrid (Sharma & Stello 2016), NumPy (Walt et al. 2011), pandas (McKinney 2010), Matplotlib (Hunter 2007), IPython (Pérez & Granger 2007), SciPy (Virtanen et al. 2020), MESA (Paxton 2020), MESA SDK (Townsend 2020), GYRE (Townsend & Teitler 2013)

REFERENCES

- Aguirre, V. S., Stello, D., Stokholm, A., et al. 2020, ApJL, 889, L34
- Ahumada, R., Prieto, C. A., Almeida, A., et al. 2020, ApJS, 249, 3
- Auge, C., Huber, D., Heinze, A., et al. 2020, AJ, 160, 18
- Baglin, A., Michel, E., Auvergne, M., & COROT Team. 2006, in ESA Special Publication, Vol. 624, Proceedings of SOHO 18/GONG 2006/HELAS I, Beyond the spherical Sun, 34.1
- Ball, W. H., & Gizon, L. 2017, A&A, 600, A128
- Balmforth, N. J. 1992, MNRAS, 255, 632
- Belkacem, K., Goupil, M. J., Dupret, M. A., et al. 2011, A&A, 530, A142
- Bellm, E. C., Kulkarni, S. R., Graham, M. J., et al. 2019, PASP, 131, 018002
- Borucki, W., Koch, D., Basri, G., et al. 2008, in IAU Symposium, Vol. 249, Exoplanets: Detection, Formation and Dynamics, ed. Y.-S. Sun, S. Ferraz-Mello, & J.-L. Zhou, 17–24, doi: [10.1017/S174392130801630X](https://doi.org/10.1017/S174392130801630X)
- Bovy, J., Rix, H.-W., Green, G. M., Schlafly, E. F., & Finkbeiner, D. P. 2016, ApJ, 818, 130, doi: [10.3847/0004-637X/818/2/130](https://doi.org/10.3847/0004-637X/818/2/130)
- Brogaard, K., Hansen, C. J., Miglio, A., et al. 2018, MNRAS, 476, 3729
- Brown, T. M., Gilliland, R. L., Noyes, R. W., & Ramsey, L. W. 1991, ApJ, 368, 599, doi: [10.1086/169725](https://doi.org/10.1086/169725)
- Buldgen, G., Rendle, B., Sonoi, T., et al. 2019, MNRAS, 482, 2305
- Chaplin, W. J., Houdek, G., Appourchaux, T., et al. 2008, A&A, 485, 813, doi: [10.1051/0004-6361:200809695](https://doi.org/10.1051/0004-6361:200809695)
- Cowling, T. G. 1941, MNRAS, 101, 367
- Cox, J. P., & Giuli, R. T. 1968, Principles of stellar structure
- de Assis Peralta, R., Samadi, R., & Michel, E. 2018, Astronomische Nachrichten, 339, 134
- El-Badry, K., Rix, H.-W., & Heintz, T. M. 2021, arXiv e-prints, arXiv:2101.05282
- Epstein, C. R., Elsworth, Y. P., Johnson, J. A., et al. 2014, ApJL, 785, L28
- Gaia Collaboration, Brown, A. G. A., Vallenari, A., et al. 2021, A&A, 649, A1
- Gaulme, P., McKeever, J., Jackiewicz, J., et al. 2016, ApJ, 832, 121
- González Hernández, J. I., & Bonifacio, P. 2009, A&A, 497, 497, doi: [10.1051/0004-6361/200810904](https://doi.org/10.1051/0004-6361/200810904)
- Green, G. M., Schlafly, E., Zucker, C., Speagle, J. S., & Finkbeiner, D. 2019, ApJ, 887, 93
- Grevesse, N., & Sauval, A. J. 1998, SSRv, 85, 161

- Grigahcène, A., Dupret, M. A., Gabriel, M., Garrido, R., & Scuflaire, R. 2005, *A&A*, 434, 1055
- Guggenberger, E., Hekker, S., Basu, S., & Bellinger, E. 2016, *MNRAS*, 460, 4277
- Hon, M., Huber, D., Kuszlewicz, J. S., et al. 2021, arXiv e-prints, arXiv:2108.01241
- Houdek, G., Trampedach, R., Aarslev, M. J., & Christensen-Dalsgaard, J. 2017, *MNRAS*, 464, L124, doi: [10.1093/mnrasl/slw193](https://doi.org/10.1093/mnrasl/slw193)
- Howell, S. B., Sobeck, C., Haas, M., et al. 2014, *PASP*, 126, 398
- Huber, D., Zinn, J., Bojsen-Hansen, M., et al. 2017, *ApJ*, 844, 102, doi: [10.3847/1538-4357/aa75ca](https://doi.org/10.3847/1538-4357/aa75ca)
- Hunter, J. D. 2007, *Computing in Science & Engineering*, 9, 90, doi: [10.1109/MCSE.2007.55](https://doi.org/10.1109/MCSE.2007.55)
- Iglesias, C. A., & Rogers, F. J. 1993, *ApJ*, 412, 752
- . 1996, *ApJ*, 464, 943
- Ivezić, Ž., Kahn, S. M., Tyson, J. A., et al. 2019, *ApJ*, 873, 111
- Jørgensen, A. C. S., Weiss, A., Angelou, G., & Silva Aguirre, V. 2019, *MNRAS*, 484, 5551
- Kallinger, T., Beck, P. G., Stello, D., & Garcia, R. A. 2018, *A&A*, 616, A104
- Kallinger, T., De Ridder, J., Hekker, S., et al. 2014, *A&A*, 570, A41, doi: [10.1051/0004-6361/201424313](https://doi.org/10.1051/0004-6361/201424313)
- Kjeldsen, H., & Bedding, T. R. 1995, *A&A*, 293, 87
- Kjeldsen, H., Bedding, T. R., & Christensen-Dalsgaard, J. 2008, *ApJL*, 683, L175
- Li, T., Bedding, T. R., Huber, D., et al. 2018, *MNRAS*, 475, 981
- Lindegren, L., Bastian, U., Biermann, M., et al. 2021a, *A&A*, 649, A4
- Lindegren, L., Klioner, S. A., Hernández, J., et al. 2021b, *A&A*, 649, A2
- Ludwig, H. G., & Kučinskas, A. 2012, *A&A*, 547, A118
- McKinney, W. 2010, in *Proceedings of the 9th Python in Science Conference*, ed. S. van der Walt & J. Millman, 51 – 56
- Miglio, A., Chiappini, C., Morel, T., et al. 2013, *MNRAS*, 429, 423
- Miglio, A., Chiappini, C., Mackereth, J. T., et al. 2021, *A&A*, 645, A85
- Mosser, B., Michel, E., Samadi, R., et al. 2019, *A&A*, 622, A76
- Mosumgaard, J. R., Jørgensen, A. C. S., Weiss, A., Silva Aguirre, V., & Christensen-Dalsgaard, J. 2020, *MNRAS*, 491, 1160
- Paxton, B. 2020, doi: [10.5281/zenodo.2602941](https://doi.org/10.5281/zenodo.2602941)
- Paxton, B., Bildsten, L., Dotter, A., et al. 2011, *ApJS*, 192, 3
- Paxton, B., Cantiello, M., Arras, P., et al. 2013, *ApJS*, 208, 4
- Paxton, B., Marchant, P., Schwab, J., et al. 2015, *ApJS*, 220, 15
- Paxton, B., Schwab, J., Bauer, E. B., et al. 2018, *ApJS*, 234, 34
- Paxton, B., Smolec, R., Schwab, J., et al. 2019, *ApJS*, 243, 10
- Pekeris, C. L. 1938, *ApJ*, 88, 189
- Pérez, F., & Granger, B. E. 2007, *Computing in Science & Engineering*, 9, 21, doi: [10.1109/MCSE.2007.53](https://doi.org/10.1109/MCSE.2007.53)
- Pinsonneault, M. H., Elsworth, Y. P., Tayar, J., et al. 2018, *The Astrophysical Journal Supplement Series*, 239, 32, doi: [10.3847/1538-4365/aaebfd](https://doi.org/10.3847/1538-4365/aaebfd)
- Pojmanski, G. 1997, *AcA*, 47, 467
- Rauer, H., Catala, C., Aerts, C., et al. 2014, *Experimental Astronomy*, 38, 249
- Rendle, B. M., Miglio, A., Chiappini, C., et al. 2019, *MNRAS*, 490, 4465
- Ricker, G. R., Winn, J. N., Vanderspek, R., et al. 2014, in *Society of Photo-Optical Instrumentation Engineers (SPIE) Conference Series*, Vol. 9143, *Society of Photo-Optical Instrumentation Engineers (SPIE) Conference Series*, 20, doi: [10.1117/12.2063489](https://doi.org/10.1117/12.2063489)
- Salaris, M., & Cassisi, S. 2005, *Evolution of Stars and Stellar Populations*
- Salaris, M., Chieffi, A., & Straniero, O. 1993, *ApJ*, 414, 580
- Serenelli, A., Johnson, J., Huber, D., et al. 2017, *ApJS*, 233, 23
- Shappee, B., Prieto, J., Stanek, K. Z., et al. 2014, in *American Astronomical Society Meeting Abstracts*, Vol. 223, *American Astronomical Society Meeting Abstracts #223*, 236.03
- Sharma, S., & Stello, D. 2016, *Asfgrid: Asteroseismic parameters for a star*. <http://ascl.net/1603.009>
- Sharma, S., Stello, D., Bland-Hawthorn, J., Huber, D., & Bedding, T. R. 2016, *ApJ*, 822, 15, doi: [10.3847/0004-637X/822/1/15](https://doi.org/10.3847/0004-637X/822/1/15)
- Sharma, S., Stello, D., Bland-Hawthorn, J., et al. 2019, *MNRAS*, 490, 5335
- Sonoi, T., Samadi, R., Belkacem, K., et al. 2015, *A&A*, 583, A112
- Stello, D., Chaplin, W. J., Basu, S., Elsworth, Y., & Bedding, T. R. 2009, *MNRAS*, 400, L80, doi: [10.1111/j.1745-3933.2009.00767.x](https://doi.org/10.1111/j.1745-3933.2009.00767.x)
- Stello, D., Zinn, J., Elsworth, Y., et al. 2017, *ApJ*, 835, 83, doi: [10.3847/1538-4357/835/1/83](https://doi.org/10.3847/1538-4357/835/1/83)
- Tassoul, M. 1980, *ApJS*, 43, 469, doi: [10.1086/190678](https://doi.org/10.1086/190678)
- Townsend, R. 2020, doi: [10.5281/zenodo.2603136](https://doi.org/10.5281/zenodo.2603136)

- Townsend, R. H. D., & Teitler, S. A. 2013, MNRAS, 435, 3406
- Trampedach, R., Aarslev, M. J., Houdek, G., et al. 2017, MNRAS, 466, L43
- Udalski, A., Szymanski, M. K., Soszynski, I., & Poleski, R. 2008, AcA, 58, 69
- Ulrich, R. K. 1986, ApJL, 306, L37, doi: [10.1086/184700](https://doi.org/10.1086/184700)
- Viani, L. S., Basu, S., Chaplin, W. J., Davies, G. R., & Elsworth, Y. 2017, ApJ, 843, 11
- Virtanen, P., Gommers, R., Oliphant, T. E., et al. 2020, Nature Methods, 17, 261, doi: <https://doi.org/10.1038/s41592-019-0686-2>
- Walt, S. v. d., Colbert, S. C., & Varoquaux, G. 2011, Computing in Science & Engineering, 13, 22, doi: [10.1109/MCSE.2011.37](https://doi.org/10.1109/MCSE.2011.37)
- White, T. R., Bedding, T. R., Stello, D., et al. 2011, ApJ, 743, 161
- Xiong, D.-r. 2021, Frontiers in Astronomy and Space Sciences, 7, 96
- Xiong, D. R., Cheng, Q. L., & Deng, L. 1997, ApJS, 108, 529
- Yu, J., Huber, D., Bedding, T. R., et al. 2018, ApJS, 236, 42, doi: [10.3847/1538-4365/aaaf74](https://doi.org/10.3847/1538-4365/aaaf74)
- Zhou, Y., Asplund, M., Collet, R., & Joyce, M. 2020, MNRAS, 495, 4904
- Zinn, J. C. 2021, AJ, 161, 214
- Zinn, J. C., Huber, D., Pinsonneault, M. H., & Stello, D. 2017, ApJ, 844, 166, doi: [10.3847/1538-4357/aa7c1c](https://doi.org/10.3847/1538-4357/aa7c1c)
- Zinn, J. C., Pinsonneault, M. H., Huber, D., et al. 2019a, ApJ, 885, 166, doi: [10.3847/1538-4357/ab44a9](https://doi.org/10.3847/1538-4357/ab44a9)
- Zinn, J. C., Stello, D., Huber, D., & Sharma, S. 2019b, ApJ, 884, 107, doi: [10.3847/1538-4357/ab43c0](https://doi.org/10.3847/1538-4357/ab43c0)